Mechanowetting drives droplet and fluid transport on traveling surface waves generated by light-responsive liquid crystal polymers

De Jong, Edwin; Kremer, Réan; Liu, Ling; Den Toonder, Jaap M.J.; Onck, Patrick R.

Published in:
Physics of Fluids

DOI:
10.1063/5.0050864

Mechanowetting drives droplet and fluid transport on traveling surface waves generated by light-responsive liquid crystal polymers

Cite as: Phys. Fluids **33**, 063307 (2021); https://doi.org/10.1063/5.0050864
Submitted: 19 March 2021 . Accepted: 21 May 2021 . Published Online: 08 June 2021

Edwin De Jong, Réan Kremer, Ling Liu (刘凌), Jaap M. J. Den Toonder, and Patrick R. Onck

Physics of Fluids ARTICLE scitation.org/journal/phf

Mechanowetting drives droplet and fluid transport on traveling surface waves generated by light-responsive liquid crystal polymers

Cite as: Phys. Fluids 33, 063307 (2021); doi: 10.1063/5.0050864
Submitted: 19 March 2021 · Accepted: 21 May 2021 ·
Published Online: 8 June 2021

View Online Export Citation CrossMark

Edwin De Jong,[1] Réan Kremer,[1] Ling Liu (刘凌),[1] Jaap M. J. Den Toonder,[2] and Patrick R. Onck[1,a)]

AFFILIATIONS

[1]Micromechanics of Materials, Zernike Institute for Advanced Materials, University of Groningen, Groningen 9747 AG, The Netherlands
[2]Department of Mechanical Engineering and Institute for Complex Molecular Systems, Eindhoven University of Technology, Eindhoven 5600 MB, The Netherlands

[a)]Author to whom correspondence should be addressed: p.r.onck@rug.nl

ABSTRACT

In nature, capillary forces are often driving microfluidic propulsion and droplet manipulation, and technologies have been developed to utilize these forces in applications such as lab-on-a-chip biosensors and microfluidic systems. At the same time, responsive materials have been developed that can be activated by a variety of external triggers, including light, electric fields, and temperature, to locally deform and create dynamic surface structures, such as traveling waves. Here, we combine these developments into a system that enables capillary-driven droplet transport and fluid propulsion generated by light-induced surface waves in azobenzene-embedded liquid crystal polymers. We demonstrate that the traveling waves are able to efficiently propel fluids by means of mechanowetting. We couple the wave profiles to the fluid simulations using a multiphase computational fluid dynamics approach. We study three different fluid propulsion systems, i.e., peristaltic flow, liquid slug transport, and free-standing droplet transport. The first system operates on a fluid-filled single channel and achieves relative flow speeds of $u/u_{wave} < 0.01$. In contrast, the slugs and droplets are transported at two orders of magnitude higher speed equal to the wave speed ($u/u_{wave} = 1$) by exploiting the mechanowetting effect. We quantify the capillary forces generated by the traveling surface waves. Our method opens new avenues in light-driven (digital) microfluidic systems with enhanced control of fluid flow.

I. INTRODUCTION

Fluid propulsion driven by capillary forces is ubiquitous in nature,[1] and it has inspired many fluid manipulation strategies in the industry, such as functional textiles for self-cleaning fabrics,[2] antiviral surface design,[3] and inkjet printing.[4] Capillary forces are also utilized in microfluidics,[5] enabling the transport of fluids by using, e.g., surface acoustic waves,[6–10] molecular motors,[11] or static wetting gradients.[12–19] Wetting gradients can also be actively controlled by applying an electric potential between the droplet and the (conducting or dielectric) substrate, as in electrowetting,[20–23] and by using materials that exhibit a chemically induced modification of the contact angle when exposed to light.[24] Additionally, electrostatic charging in combination with a superhydrophobic surface can be used to switch the mobility of droplets by controlling the different wetting states.[25] However, these methods also have downsides, such as unwanted byproducts as a result of electrochemical reactions, the requirement of a fully integrated electronic circuit on the chip in the case of electrowetting and the limited contact angle range in the case of chemical wetting control.

As an alternative to the existing methods, we recently proposed to use mechanical deformation to locally control the wetting gradient.[26] This so-called "mechanowetting" effect is based on surface deformation-controlled three-phase line motion that can be used to transport fluid slugs in microchannels[27] and individual droplets on surfaces with high speed and precision.[26] Surface deformation gradients can be induced by using responsive materials that can be externally controlled by, e.g., light,[28–30] temperature,[31] electric fields,[32] or magnetic fields.[33,34] Based on its scalable and precise spatial-temporal control, light often is an attractive external trigger compared to electric, magnetic, and thermal actuation. For example, Lv and co-workers reported the propelling of fluid slugs in tubes functionalized with photo-responsive liquid crystal polymers,[35] and Li and co-workers

generated droplet-propelling dielectrophoretic forces in a trilayer structure with a near-infrared laser beam.[36] However, the current setups include complex structured lenses, masks, and mirrors and often require a moving light source.[35–39] We have tried to tackle these challenges by generating continuous, mechanical surface waves by using azobenzene-modified liquid crystal coatings that are responsive to a uniform UV light source.[40] By tuning the molecular order and by controlling the polarization direction of the UV light, the *trans*-to-*cis* isomerization process is selectively activated, which induces a spatial distribution of macroscopic deformation. By doing so, a dynamic surface wave is created by rotating the polarization direction of the UV light.

In the current work, we use the recently developed numerical and theoretical frameworks[26,27] to demonstrate that these light-induced surface waves can effectively propel fluid slugs and droplets at the speed of the wave by means of mechanowetting. We use the light-driven traveling waves developed in earlier work[40] to manipulate individual droplets and fluid slugs in microchannels based on manipulation of the three-phase line and compare their efficiency with standard peristaltic motion. We show how the wave properties are sufficient to propel droplets and how fluid transport efficiency depends on the properties of the used films.

II. METHODS

The films used in this study are liquid crystal polymers, modified with azobenzene molecules. When these films are exposed to polarized UV light, the embedded azobenzene molecules isomerize from a rod-like *trans* state into a bent-like *cis* state [Fig. 1(a)], which introduces a structural disorder in the thin film, leading to a mechanical response that shapes the surface profile.[28,41,42] The propensity of the azobenzene molecules to make this transition is determined by the average orientation $\boldsymbol{n}$ (the director) of the molecules with respect to the electric field $\boldsymbol{E}$ of the polarized UV, i.e., $\boldsymbol{n}\cdot\boldsymbol{E}$. Here, $\boldsymbol{n}$ is implemented as a continuum property, i.e., the statistical fluctuations in orientation at the molecular scale are averaged out [see Fig. 1(a)]. The photo-induced surface topographical changes of the liquid crystal films and the traveling wave generation are simulated via an optomechanical framework,[28,41,42] following the protocol established in our previous work (Ref. 41) by using a rotating polarized filter. The key geometrical variables are the wavelength of the director pattern in the plane of the film [see Figs. 1(b)–1(d) and 2] denoted by λ, and the film thickness w, whose ratio λ/w determines the mechanical interactions between the different regions and thus affects the wave amplitude.[40] Details of the modeling, design, and optimization of the traveling surface waves in the liquid crystal film can be found in Refs. 40 and 42. For completeness, we briefly summarize the approach here. The director distribution is periodically varied spatially [a single wavelength is shown in Fig. 1(b)]. When the surface is illuminated by the polarized UV light, the *cis*-to-*trans* conversion at different regions of the surface is proportional to $|\boldsymbol{E}\cdot\boldsymbol{n}|$. For example, the cases for $\phi = 90^\circ$ and $\phi = 45^\circ$ in Fig. 1(c) show that a different polarization direction creates a different surface topography. Rotating the electric field clockwise from $\phi = 90^\circ$ to $\phi = 45^\circ$ results in the wave-like profile traveling to the right [Fig. 1(b)]. Because of the periodic design of the director distribution, every polarization direction (i.e., $0^\circ \le \phi < 180^\circ$) generates a unique topography that has a wave-like form, and a small change in ϕ will translate to a small phase-shift. Thus, a traveling wave is generated by rotating the polarization direction.

In the current study, we consider three different applications of induced fluid motion by means of the switchable surface. In the first application, we apply the traveling wave topography to a microfluidic wall in an infinitely long microchannel, filled with a single fluid [Fig. 2(a)]. At the inlet and outlet of the microchannel, we apply periodic boundary conditions. For the second application, a second fluid is added to the microchannel, immiscible with the first fluid, which allows us to generate fluid slugs [see Fig. 2(b)]. Finally, we consider single, free-standing droplet transport [see Fig. 2(c)]. Again, periodic boundary conditions are imposed on the inlet and the outlet of the simulation domain. Figure 2 schematically depicts all system variables.

In order to characterize the generated waves and to quantify the fluid motion on our liquid crystal films, the relevant surface and fluid parameters are normalized as follows. The mean velocity of the fluid $\bar{u}$ is normalized by the wave speed of the switchable surface topography $u_{\text{wave}} = \lambda f$, that is $\bar{u}/u_{\text{wave}}$, which is the inverse of the Strouhal number, St^{-1}. In order to distinguish between the different switchable surfaces, λ/w, i.e., the ratio between the wavelength and the film thickness, is used. The amplitude of the surface wave is nondimensionalized as A/λ, where the amplitude A is half the difference between the maximum and minimum expansions of the substrate across all polarization angles. Finally, the width and diameter of the fluid slugs and droplets are nondimensionalized as L/λ and d/λ, respectively. The forces generated by the traveling waves are quantified by $\Delta p h_0/\gamma_{\text{lv}}$ for the slugs, and $F/\gamma_{\text{lv}}d$ for the droplets, respectively. The remainder of the parameters shown in Fig. 2, the fluid density ρ, the fluid viscosity μ, the (mean) microchannel height h_0, and the solid film thickness w (when not exposed to UV light), is not studied in detail. The subscripts A and B distinguish between the different fluids in the channel.

A. Fluid simulations

The fluid computations were performed based on the OpenFOAM framework, using the volume-of-fluid multiphase formulation of the Navier–Stokes equations, i.e.,

$$\frac{\partial \rho \boldsymbol{u}}{\partial t} + \nabla\cdot(\rho\boldsymbol{u}\boldsymbol{u}) = -\nabla p + \rho\boldsymbol{g} + \nabla\cdot\left[\rho\mu(\nabla\boldsymbol{u} + (\nabla\boldsymbol{u})^{\top})\right] + \rho\gamma_{\text{lv}}\kappa\nabla\alpha,$$
$$\frac{\partial \rho}{\partial t} + \nabla\cdot(\rho\boldsymbol{u}) = 0,$$
$$\frac{\partial \alpha}{\partial t} + \nabla\cdot(\alpha\boldsymbol{u}) = -\nabla\cdot(\boldsymbol{u}_{\text{r}}\alpha(1-\alpha)).$$

Here, ρ is the fluid density, $\boldsymbol{u}$ the fluid velocity, p the pressure, $\boldsymbol{g}$ the gravitational acceleration vector, μ the viscosity, γ_{lv} the surface tension, κ the fluid–fluid interface curvature (i.e., liquid–air for the droplet simulations and liquid–liquid for the slug simulations), α the indicator field that distinguishes between the two fluids, and $\boldsymbol{u}_{\text{r}}$ an artificial relative velocity that ensures that the interface remains sufficiently thin and does not smear out.[43] The properties of the two fluids in each simulation (viscosities μ_{A}, μ_{B} and densities ρ_{A}, ρ_{B}) are implemented through the indicator field α by linear combination, i.e.,

$$\mu \equiv \mu_{\text{A}}\alpha + \mu_{\text{B}}(1-\alpha),$$
$$\rho \equiv \rho_{\text{A}}\alpha + \rho_{\text{B}}(1-\alpha).$$

Here $\alpha = 1$ represents fluid A, and $\alpha = 0$ represents fluid B. The interface between the two fluids is located in the cells where $0 < \alpha < 1$.

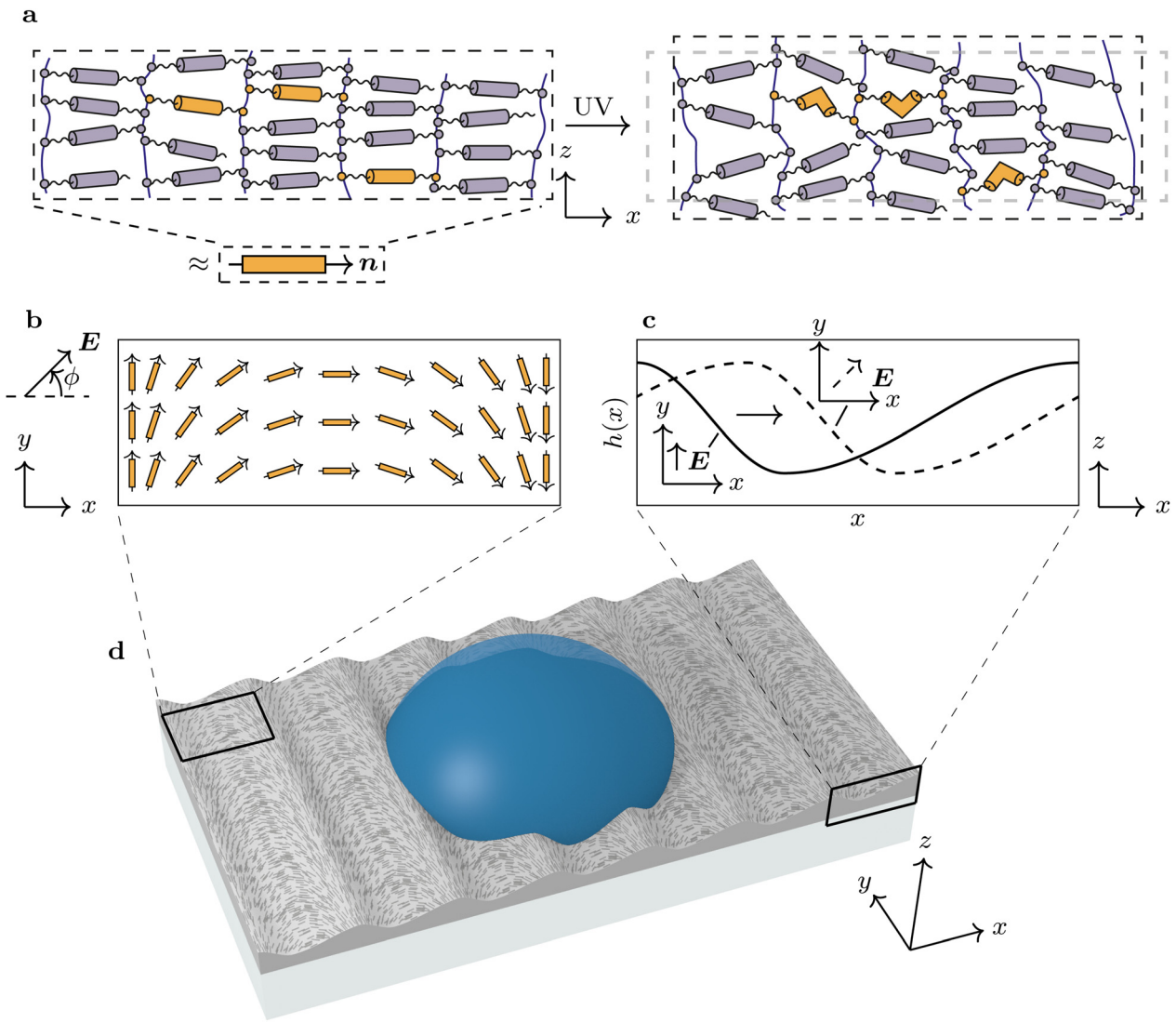

FIG. 1. Droplet propulsion by polarization-controlled surface waves and mechanowetting. (a) An illustration of the isomerization of azobenzene molecules (orange) embedded in the liquid crystal polymer (purple) from the rod-like *trans* state to the bent-like *cis* state when exposed to (polarized) UV light. The average orientation of the azobenzene and liquid crystal molecules is the (continuum) director ***n***. (b) Spatial variation of the orientation of the director in the *x*, *y* plane of the solid film. The electric component of the polarized UV light (***E***, left) is rotated in that same plane. (c) Two different orientations of ***E*** in the *x*, *y* plane (inset) and the corresponding surface height profiles *h*(*x*) in the *x*, *z* plane. (d) Graphical overview of a single droplet that is being propelled by mechanowetting on the generated traveling wave. The fine texture indicated on the surface of the film denotes the in-plane director distribution corresponding to (b).

The single-phase fluid simulations were performed with a similar model. However, since only one fluid and no interface is present in the channel, all terms containing α are zero.

In order to reduce the spurious velocities near the fluid–fluid interface that originates from the calculation of the interface curvature κ, we based the interface calculation on a smoothed indicator field. This allows us to accurately simulate μm-sized slugs and mm-sized droplets.[44] We have studied mesh convergence and found that in order to obtain converged results, the mesh resolution needed to be sufficiently small, i.e., $\Delta x = 10\,\mu$m for the droplets, and $\Delta x = 2.5\,\mu$m for the channels. To satisfy the Courant–Friedrichs–Lewy condition for convergence, the time steps were set to $\Delta t = 2.5$ and $\Delta t = 1$ ms for the droplets and channels, respectively. As we showed in earlier work, the numerical model shows close correspondence to the experimental results.[26] More details on the computational method can be found in Refs. 43–45.

The wave boundaries used in this study were implemented as a deforming mesh boundary condition and to ensure the periodicity of the wave, the height profiles resulting from the solid simulations were Fourier interpolated, i.e.,

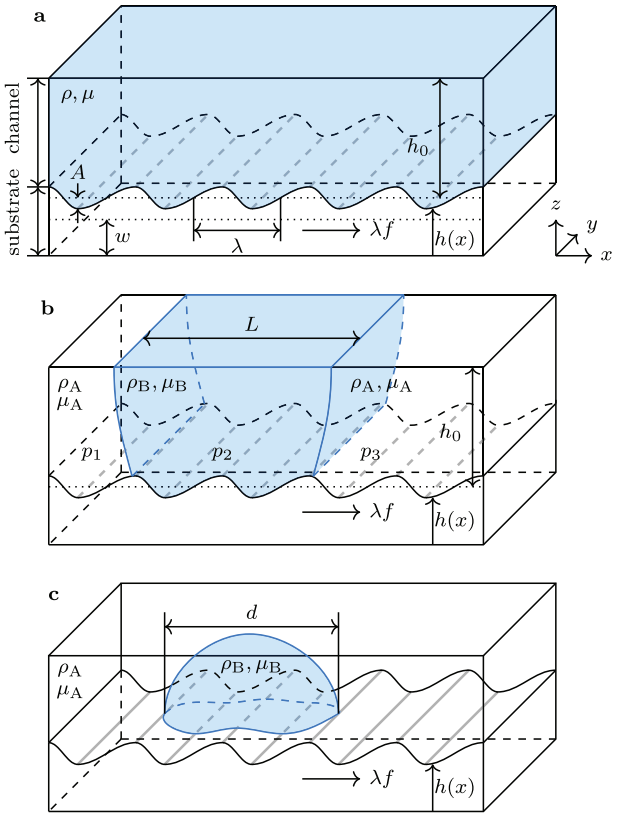

FIG. 2. Schematics illustrating the fluid motion in this study and its parameters. (a)–(c) Schematics for the simulation domains of the studied cases for (a) a channel filled with a single fluid, (b) a channel filled with a fluid slug, and (c) a single droplet in air.

$$h(x) \approx A\left[a_0 + \sum_{n=1}^{m} a_n \cos\left(\frac{2\pi x}{n\lambda}\right) + b_n \sin\left(\frac{2\pi x}{n\lambda}\right)\right], \qquad (1)$$

where a_n and b_n are normalized proportionality constants and m was taken to be equal to 8 as the Fourier order used for the surface profiles. For each surface, the surface profiles for 16 different polarization angles were simulated, using cubic splines to interpolate between the 16 profiles to obtain surface profiles at any given time. During the calculation of each time step in the fluid simulations, the mesh boundary points are moved according to the profile of Eq. (1) and the rest of the mesh is updated according to an artificial diffusion law in order to preserve mesh quality.[46] To ensure smooth mesh transitions, the mesh points at the top of the domain are fixed, and the mesh points on the sides of the simulation domain are given a slip boundary condition, i.e., those mesh points are able to move freely parallel to the boundary. At this deforming boundary, the fluid velocity field is equal to the deformation velocity (i.e., no slip and no flux) in order to preserve the (droplet) volume. The artificial diffusion law can be used because the deformations (amplitudes) are very small. Note that the horizontal velocity was assumed to be zero, since the lateral deformation of the constrained films was observed to be much smaller than the vertical deformation.

For the remainder of the computed fields, we have prescribed the following boundary conditions. On the deforming surface, the contact angle is implemented by prescribing the gradient of the indicator field α, and the pressure p is adapted to accommodate the zero flux. For the slug simulations [Fig. 2(b)], we employ two types of boundary conditions. The first is an infinite channel with periodic boundary conditions, similar to the single-fluid simulations [Fig. 2(a)]. The second is a closed-channel approach that closes the channel on the right-hand side to allow for pressure to build up. By doing so, we are able to quantify the pressures that the surfaces can generate. The top of the channel is equipped with no slip and no flux boundary conditions, and a contact angle of 90°. In the 3D droplet simulation, the side walls are equipped with slip and zero flux boundary conditions, and the indicator field is fixed at $\alpha = 0$ (i.e., air). The top of the simulation domain is a mixed boundary condition, where the velocity is adjusted to the inward flux normal to the boundary in the case of inflow, and a zero gradient condition is applied in the case of outward flow.

B. Pressure modeling in slugs

In this section, we summarize the theoretical pressure modeling of slugs in a closed channel and extend the theory to account for the surface structure defined in Eq. (1). For details, the reader is referred to Ref. 27. The distance from the three-phase line (located at position x) to the top of the channel can be expressed using

$$\delta(x) = h_0 - h(x).$$

The curvature of the interface is assumed to be circular, such that it can be expressed as

$$\frac{1}{R(x)} = \frac{\sin\beta(x)}{\delta(x)},$$

where $\beta(x)$ is defined as the local inclination at the three-phase line, i.e.,

$$\beta(x) = \arctan\left(\frac{d\delta}{dx}\right) - (-1)^n\left(\theta_Y - \frac{\pi}{2}\right).$$

Here, $n = 1$ or 2 is the index of the left or right interface (see Fig. 2), which is used to account for the sign of the Laplace pressure jump. Now, by accounting for constant volume of the slug (Lh_0 is the slug volume per unit depth), we obtain

$$Lh_0 = \frac{R_1^2}{4}(2\beta_1 - \sin(2\beta_1)) - \frac{R_2^2}{4}(2\beta_2 - \sin(2\beta_2)) + \int_{x_1}^{x_2} \delta(x)\,dx, \qquad (2)$$

where x_1 and x_2 are the locations of the left and right interfaces, respectively. Note that, $R_i \equiv R(x_i)$ and $\beta_i \equiv \beta(x_i)$ were substituted for clarity. Equation (2) can be solved for x_2 if x_1 is known (since Eq. (1) is periodic, $x_1 \in [0, \lambda]$ is sufficient to capture all possible states), by using a (numerical) root finding algorithm. The total pressure difference that is built up over the slug can finally be calculated using the Laplace equation, i.e.,

$$\Delta p(x_1, x_2) = \gamma_{lv}\left(R_1^{-1} + R_2^{-1}\right). \qquad (3)$$

C. Mechanowetting three-phase line integral theory

In this section, we summarize the mechanowetting three-phase line theory. For details, the reader is referred to Ref. 26. The dynamic-pinning forces generated by the mechanowetting mechanism are calculated from the collaborative contributions of the distortions to the Young equation[47] at each point of the three-phase line. When the Young equation is distorted due to the deformation of the liquid crystal film (i.e., the contact angle is perturbed by an amount such that $\theta_Y \rightarrow \theta_Y + \Delta\theta$), a force per unit length is generated, which can be written as[26]

$$\boldsymbol{f} = \boldsymbol{n}_t \gamma_{lv} \sin\theta_Y \Delta\theta,$$

where $\boldsymbol{n}_t$ is the unit vector normal to the three-phase line in the horizontal plane. When integrated over the full three-phase line (TPL), we obtain the total force that originates from the distortions, i.e.,

$$\boldsymbol{F} = \oint_{TPL} \boldsymbol{f}\, ds.$$

When we consider a deforming surface, the change in surface topography from flat to corrugated leads to a distortion of the contact angle,

$$\Delta\theta = \arctan[\boldsymbol{n}_t \cdot \nabla h].$$

For small distortions, the three-phase line can be approximated as a circle, so that the line integral from Sec. II C, after nondimensionalization of the forces using the surface tension γ_{lv} and the droplet diameter d, reduces to

$$\frac{\boldsymbol{F}}{\gamma_{lv} d} = \frac{\sin\theta_Y}{2} \int_0^{2\pi} \boldsymbol{n}_t \arctan[\boldsymbol{n}_t \cdot \nabla h]\, d\varphi, \tag{4}$$

where φ is the angular component of the transformation to the polar (cylindrical) coordinate system (i.e., $x = 0.5d\cos\varphi$, $y = 0.5d\sin\varphi$).

III. RESULTS

A. Peristaltic propulsion of single-phase fluids

Patterning azobenzene molecules nonuniformly in the x, y plane of a liquid crystal polymer film allows us to create sinusoidal-like periodic topographies on the liquid crystal surface upon exposure to polarized UV light (see Fig. 1). By rotating the polarization in the counterclockwise direction, a surface wave that travels in the positive x-direction (i.e., to the right in the figure) is created. In this paper, eight of such surfaces are investigated by varying the thickness of the film, resulting in different values of λ/w, evenly distributed between $\lambda/w = 2$ and $\lambda/w = 16$. Figure 3(a) shows the progress of one wave due to a rotating polarization angle for $\lambda/w = 2$; the waves for the other λ/w values can be found in the supplementary material. The period of the surface wave $\Delta\phi$ is equal to 180°.

The traveling surface waves generated through the rotating polarized UV light source are then applied to an infinitely long microfluidic channel. The surface waves are applied as dynamic boundary conditions to a computational fluid dynamics (CFD) model of the channel. The simulations are carried out by using the open-source CFD solver OpenFOAM. For details of the numerical implementation, the reader is referred to Sec. II. The deformations introduced in the switchable surface by the rotating polarization angle induce a nonuniform pressure field and fluid velocity in the channel [see Fig. 3(b)]. The resulting high- and low-pressure areas are a result of the upward and downward motions of the surface topography, respectively. These differences in pressure induce a predominantly forward velocity in the fluid, i.e., a velocity in the same direction as the wave speed, as can be observed from the streamlines plotted in Fig. 3(b). There is also some backflow in the system, where fluid flows against the direction of the wave. To quantify the fluid propulsion, the resulting fluid velocity is averaged over a vertical cross section, denoted by V in Fig. 3(b), and shown in Fig. 3(c). The backflow in the system can be clearly seen; as for certain values of ϕ, the velocity is negative. However, when integrating the velocity over a single period, it becomes apparent that this backflow is smaller than the forward flow, resulting in a positive net flow $\bar{u}$ to the right [see Fig. 3(d)]. The normalized mean velocity over a single period ($\bar{u}/u_{wave}$) is largest for small λ/w, since this configuration generates the highest values for A/λ, the normalized amplitude of the waves. Using the switchable surface to drive the fluid flow in a channel, average fluid velocities are generated that are on the order of $\sim 10^{-3}$ smaller than the wave velocity and therefore have an efficiency of around 0.1%.

Finally, the fluid velocities are compared to the theoretical results from Taylor,[48] who modeled a free-standing, undulating film swimming in a liquid bath. The normalized swimming velocity was found to be proportional to A^2/λ^2, in the case of a purely sinusoidal wave. By modeling our surfaces with a scaled amplitude, we found that Taylor's scaling law also holds for our surfaces, as expected. This can be seen in Fig. 3(e). Here, the solid squares represent simulations in which the amplitude was artificially lowered compared to the open circles. Other than the scaled amplitude, the dotted lines connecting the circles and squares denote that the surface topography is the same.

B. Microfluidic slug transport

Next, we analyze the situation in which we insert a slug of a different fluid (fluid B) that is immiscible with the original fluid A [see Fig. 2(b)]. The interfaces separating these fluid slugs intersect with the switchable surface, creating a three-phase contact line. As the surface deforms and the wave travels, the fluid interface adjusts its orientation to the slope of the surface topography, to maintain the equilibrium contact angle. This changed orientation of the interface near the contact line causes the full interface to become curved, generating a Laplace pressure. A force proportional to this pressure jump drives the slug in the direction of the wave.[27] As the wave travels further, the slugs are transported through the channel at the wave speed u_{wave} [see Fig. 4(a)].

To estimate the forces generated by mechanowetting, we examined the pressure difference the traveling waves can impose on the fluid slugs. To this end, we close the channel at the right and open it at the left and examine the buildup of the pressure as the surface wave travels to the right. Figure 4(b) shows the difference between the pressure in the closed compartment at the right and the open compartment at the left, $\Delta p = p_3 - p_1$. From Fig. 4(b), it becomes clear that the configurations with the lowest and highest pressure differences only appear once per period. It turns out that the maximum pressure difference that the surface can generate depends on the polarization angle ϕ. However, in addition to the polarization dependence, the pressure difference also depends on the position of the fluid interfaces on the liquid crystal coating [as is shown in Fig. 4(b)]. This is because the surface topography at different values of the polarization angle can

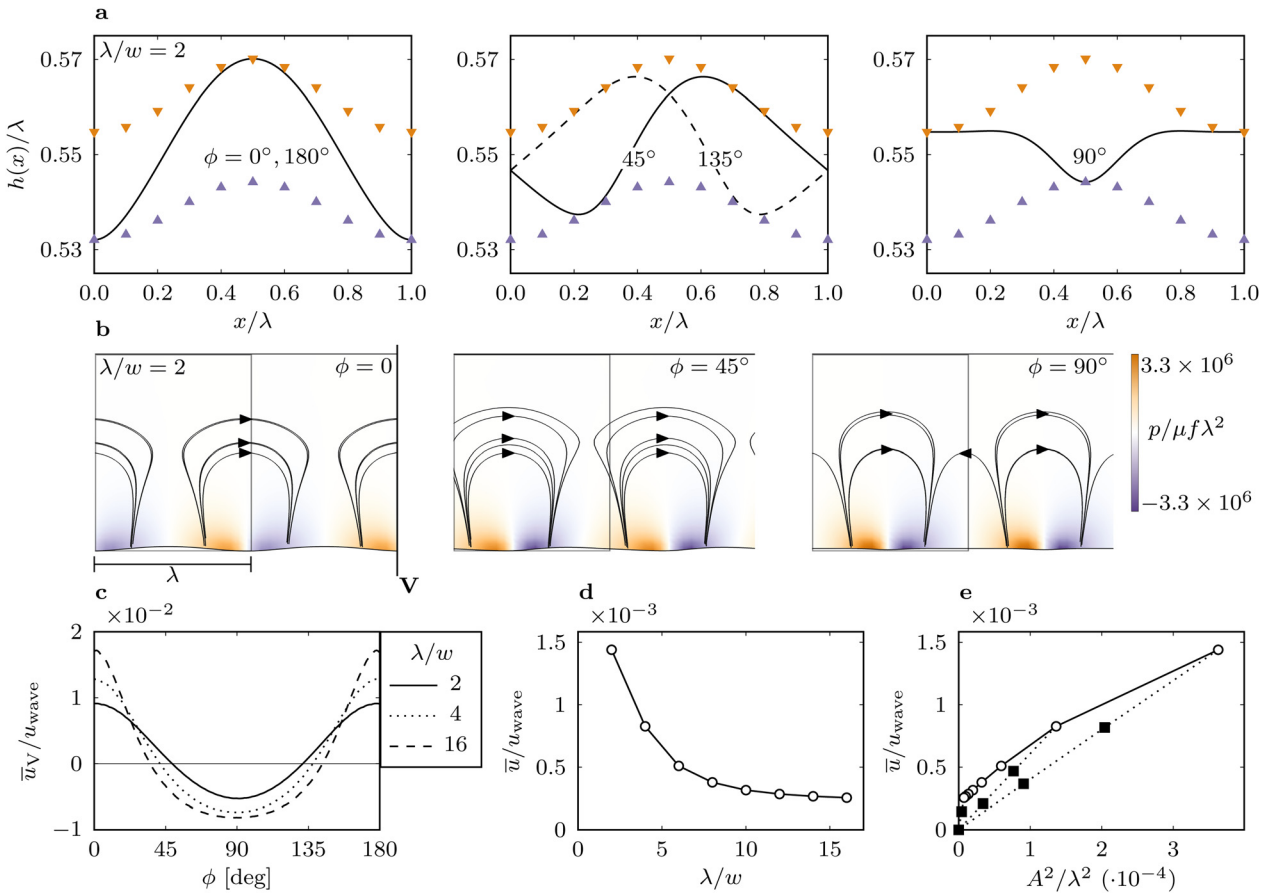

FIG. 3. Wave generation on azobenzene-modified liquid crystal coatings and the resulting peristaltic motion. (a) The normalized surface height h/λ for various polarization rotation angles ϕ, for a surface topography corresponding to $\lambda/w = 2$. The orange and purple triangles indicate the highest and lowest points for that specific location x, respectively, overall values of ϕ. (b) Snapshots of the pressure distribution in the fluid for the peristaltic movement in a channel corresponding to the same rotation angles as used in (a). The wave amplitude is amplified two times to emphasize the shape of the surface topography. (c) Normalized mean velocity $\bar{u}/u_{wave}$ through the cross-sectional area denoted by the vertical line V, as outlined in (b), for different orientations ϕ and for various values of λ/w. (d) Mean velocity ($\bar{u}$), averaged over a single period (i.e., $0^\circ \leq \phi \leq 180^\circ$), normalized by u_{wave}, for various values of λ/w. (e) Normalized mean velocity as a function of the normalized amplitude. Here, the open circles mark the same results as shown in (d), and the solid squares represent similar simulations with a scaled amplitude. The dotted lines connect the squares and circles that represent the same surface wave with scaled amplitudes.

be slightly different. To analyze this, the simulation of Fig. 4(b) is repeated for different locations of the center of mass x_{CM}, see Fig. 4(c). Here, the polarization angles of the simulations are phase shifted by $180^\circ x_{CM}/\lambda$ for a clearer visualization (see the supplementary material for the original data). During each run, for a slug fixed at a specific value of x_{CM}/λ, the pressure difference generated develops in a similar fashion as in the pressure graph shown in Fig. 4(b), but it is shifted vertically and horizontally (see the supplementary material). To determine the range of pressures that can be generated by the system, i.e., the transporting efficiency, we use these pressure graphs from the closed-channel configuration and project them on the infinite-channel situation. Suppose the fluid slug travels to the right through the channel and at a given point in time, it experiences resistance to transport (e.g., due to surface heterogeneities or an applied counter pressure). Consequently, the slug will remain stationary while the wave travels underneath, i.e., the slug's center of mass x_{CM} is fixed in place. While the wave travels underneath, a driving force is generated by the surface waves, which, depending on where the slug is trapped, will follow one of the graphs shown in Fig. 4(c). If at a certain value for the polarization angle ϕ, the builtup pressure is large enough to overcome the resistance, and the slug will reattach to the wave and proceed to travel at the wave speed. If the maximum counter pressure due to the resistance is larger than the maximum possible driving pressure generated by the surface for the location x_{CM} at which the slug was trapped, the slug will stall. Therefore, the maxima of the curves in Fig. 4(c) represent the maximal driving pressures that can be generated for each x_{CM}/λ. This range is marked by the thick vertical bar in Fig. 4(c). Note that the ability to overcome resistance for the system as a whole must be taken as the worst-case scenario, i.e., the lower limit of this range, as it is not possible to predict at which location the slug will be trapped. This is highlighted by the circle in Fig. 4(c). We repeated this analysis for different values of λ/w and plotted the range of driving pressures

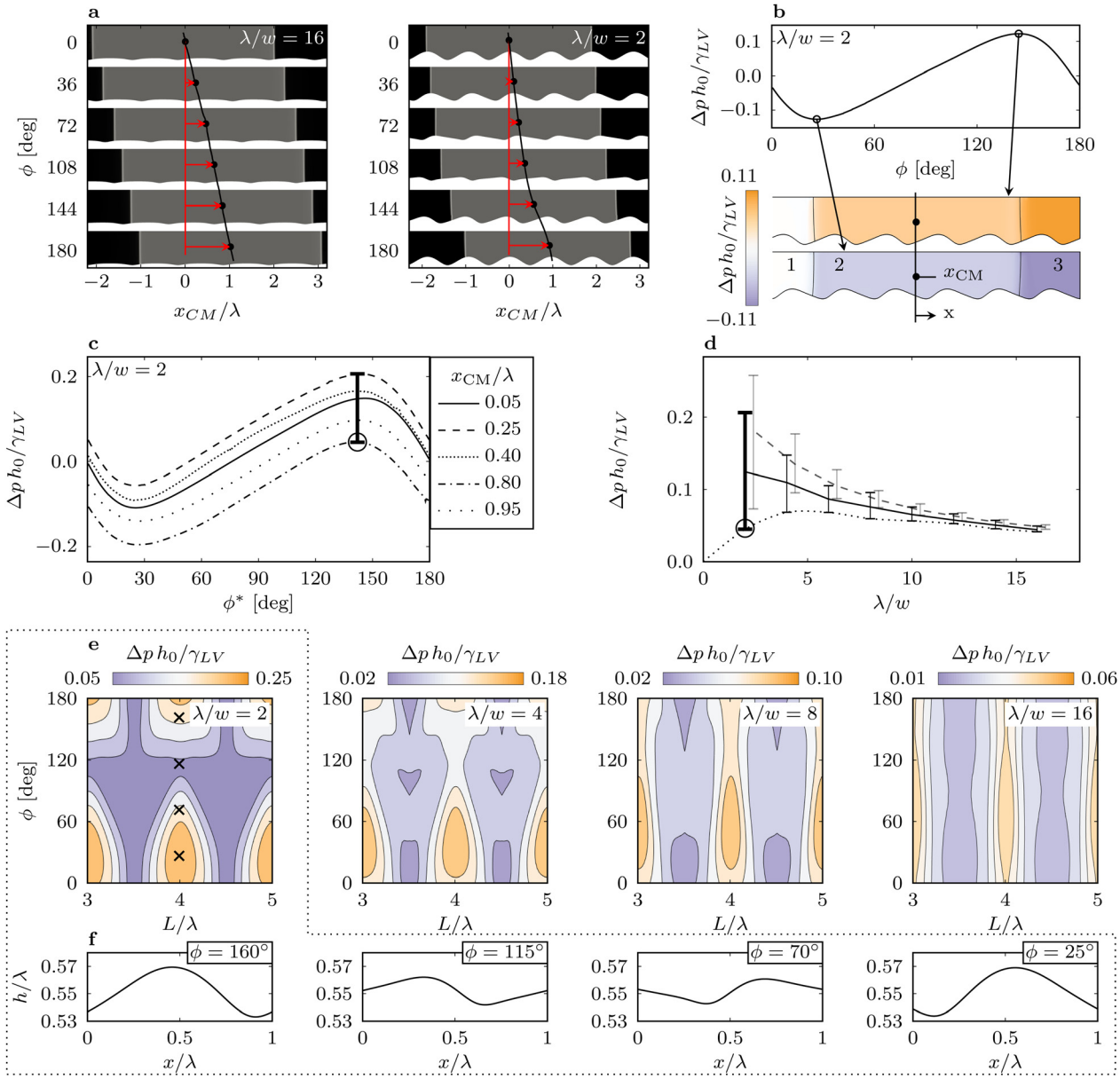

FIG. 4. Slug transport on liquid crystal traveling-wave surface topographies. (a) Normalized distance traveled by the slug (indicated by the red arrows that depict the motion of the center of mass, x_{CM}), as a function of the polarization angle ϕ at steady state for $\lambda/w = 16$ and $\lambda/w = 2$, for fluid slugs of size $L/\lambda = 4$. The wave amplitude in the snapshots is amplified five times to emphasize the difference in shape of the surface topography between $\lambda/w = 2$ and 16 and for different values of ϕ. (b) (top): $\Delta p\, h_0/\gamma_{LV}$ (with $\Delta p = p_3 - p_1$) as a function of the polarization angle for a closed channel for $\lambda/w = 2$ for fluid slugs of size $L/\lambda = 4$ at position $x_{CM}/\lambda = 0$. (bottom): Pressure distribution in the channel at two different values of the polarization angle ($\phi = 25^\circ$ and 145°), corresponding to the maximum and minimum pressures. The wave amplitude is amplified five times to emphasize the shape of the surface topography. (c) $\Delta p\, h_0/\gamma_{LV}$ as a function of the polarization angle for $\lambda/w = 2$ and $L/\lambda = 4$ for different initial positions of the slug, denoted by the initial center of mass position x_{CM} as shown in (a) and (b) (bottom). The graphs have been horizontally displaced (i.e., $\phi^* = \phi - 180^\circ x_{CM}/\lambda$) to align the maxima for clarity (see the supplementary material for the original data). The thick vertical bar highlights the range of maximal $\Delta p\, h_0/\gamma_{LV}$ that the surface can generate, whereas the circle mark emphasizes the lower limit of this range. (d) Mean $\Delta p\, h_0/\gamma_{LV}$ for fluid slugs of size $L/\lambda = 4$ for various values of λ/w obtained both numerically (solid) and analytically (dashed). The vertical bars denote the maxima and minima as shown in (c) and the thick vertical bars with the circle mark the same region detailed in (c). The dotted line connects the minima, i.e., the actual efficiencies of the different surfaces. The analytical solution is displaced horizontally by $\lambda/w = 0.4$ for clarity. (e) $\Delta p\, h_0/\gamma_{LV}$ as a function of ϕ and L/λ for $\lambda/w = 2, 4, 8$, and 16, calculated using the analytical model. (f) Surface topography of a single wave corresponding to $\phi = 25^\circ, 70^\circ, 115^\circ$, and 160° for $\lambda/w = 2$, corresponding to the crosses in (e).

for different values of λ/w in Fig. 4(d) [the thick vertical bar coincides with Fig. 4(c)]. The dotted line connects the minimal driving forces. From this, we conclude that $\lambda/w = 4$ is the optimal switchable surface for slug flow in a real system, since the minimum driving force peaks at that value.

We applied an analytical model to support the results of the simulations, based on the Laplace pressure difference generated by cylindrical slug end-caps described by Eq. (3).[27] The results generated by the analytical model compare reasonably well with the numerical results [see Fig. 4(d)], with relative errors around 30% for $\lambda/w = 2$, decreasing to 7% for $\lambda/w = 16$. Note that the trend is represented accurately, which indicates that we have captured the essential physics in the analytical model. Consequently, we use the analytical model to determine the dependence of the efficiency on the slug size L. Here, a similar approach was followed as for Fig. 4(d). However, in order to show that the driving pressure generated by the slug in the channel varies with the applied polarization angle ϕ, we analyzed the slug at specific values for ϕ and determined the maximum driving pressure by varying x_{CM}/λ. By doing so for $0° \leq \phi \leq 180°$ and $3 \leq L/\lambda \leq 5$ and plotting a Δp contour in Fig. 4(e), it becomes clear that for integer values of L/λ, the normalized pressure differences are highest for all λ/w and polarization angles. It also becomes apparent that the generated pressure profiles in Fig. 4(e) are considerably different for the different values of λ/w. For $\lambda/w = 16$, the magnitude of the normalized pressure is nearly independent of the rotation angle ϕ of the polarization angle. This is because the shape of the surface corrugation barely changes as a function of the polarized light for this thin film (see the supplementary material). Conversely, for $\lambda/w = 2$, there are large differences in the normalized pressure difference as a function of the polarization angle, which is due to the large differences in surface topography when cycling through the different orientations of the polarization angle [see Fig. 4(f) and the supplementary material].

C. Droplet transport

Finally, switchable surfaces are used to transport single droplets. We deposit a droplet on the switchable surface in the flat (i.e., "dark") configuration. When the UV light is switched on, the film attains its corrugated state and the droplet moves toward its equilibrium position, which is with the three-phase line as close as possible to the crests of the wave.[26] When the polarized light source is rotated, the droplet is transported at the same velocity as the traveling waves [see Fig. 5(a)], in a similar manner as the fluid slug [see Fig. 4(a)]. For the slugs, we were able to directly quantify the force generated by measuring the pressure drop over the closed channel, but this is not possible for the droplet. Instead, a body force is applied to the droplet in a direction opposite to the traveling direction of the wave. During the simulation, this force is slowly increased, until the droplet detaches from the dynamic corrugations and moves in the direction of this force. The force at the moment of detachment marks the maximum "dynamic-pinning" force that the surface topography is able to exert on the droplet.

Considering that the surface topography is different for different film thickness (i.e., λ/w) and different polarization angles of the UV light [see Figs. 3(a) and 4(f) and the supplementary material], the maximum of the dynamic-pinning force for a specific droplet size d and film thickness λ/w depends on the polarization angle at the moment the droplet detaches from the surface. To quantify this, we determined the dependence of the dynamic-pinning force on the droplet size d, for the specific surface profile associated with a polarization angle ϕ and film thickness λ/w. Figure 5(b) shows this for $\lambda/w = 16$ and $\phi = 150°$. Here it becomes clear that the droplet size d plays a significant role in the resulting maximum dynamic-pinning force, similarly to the size L of the fluid slugs.

The numerical results are compared to an analytical model that is described in Eq. (4).[26] This theory calculates the tension on the base of the droplet as a result of the dynamic change of the surface and integrates these to calculate the resulting force on the droplet. In Fig. 5(b), the theoretical results (solid lines) are plotted next to the numerical results (crosses), showing that the theoretical model yields results that are consistent with those generated by the numerical model with relative errors of 10% on average (maximally 25%). Note that this is in line with the experimental trend found in Ref. 26 and that the trend is represented accurately. Subsequently, this analytical model is used to study the dynamic-pinning force as a function of droplet size d/λ, film thickness λ/w, and polarization angle ϕ. We analyzed the transportation efficiency by modeling the surfaces for various film thicknesses at a relative droplet size $d/\lambda = 3.2$. By varying the polarization angle ϕ, we determined the range of possible dynamic-pinning forces of the droplet on these surfaces. The vertical bars in Fig. 5(c) show the range of the dynamic-pinning forces, with every point in the range corresponding to different polarization angles. Again, the point of interest is the lower bound of the force, showing that the ideal surface topography for droplet transport is $\lambda/w = 4$, similar to the transport of fluid slugs [Fig. 4(d)].

The analytical model is used to determine the dependence of the pinning force on the size of the droplet and on the polarization angle for different film thicknesses λ/w [Fig. 5(d)]. In a similar manner to the slugs, this was done by displacing the droplet at fixed ϕ to determine the maximum driving force for that polarization angle. Here it becomes clear that for higher values of λ/w, the dependence of the magnitude of the driving force on the polarization angle decreases, similar to the slug flow. This can be explained by the fact that the shape of the surface corrugations corresponding to $\lambda/w = 2$ changes drastically with polarization angle, whereas the surface topography corresponding to $\lambda/w = 16$ barely changes (see the supplementary material). Figure 5(e) shows the tensions along the three-phase line for different values of the polarization direction for $\lambda/w = 2$, corresponding to the crosses in Fig. 5(d) (left image). It can be seen that the tensions on the base of the droplet are nonuniform and do not always point in the direction of the wave, resulting in a strong variation of the net driving force with polarization angle [see Fig. 5(d)]. However, when integrated over the three-phase line, the tensions result in a dynamic-pinning force that is pointed in the desired direction of transport (red arrows).

IV. DISCUSSION

The traveling wave surface topographies are capable of displacing fluid slugs in enclosed channels as well as transporting free-standing droplets. Although the areas of application are different, the physical principle behind the fluid propulsion for both cases, i.e., mechanowetting, is the same, resulting in the three-phase line pinning to the crests of the traveling waves. For the fluid slugs, we quantified the performance theoretically by calculating the Laplace pressure from the interface curvature (see Ref. 27 and Sec. II), while for the droplets, the

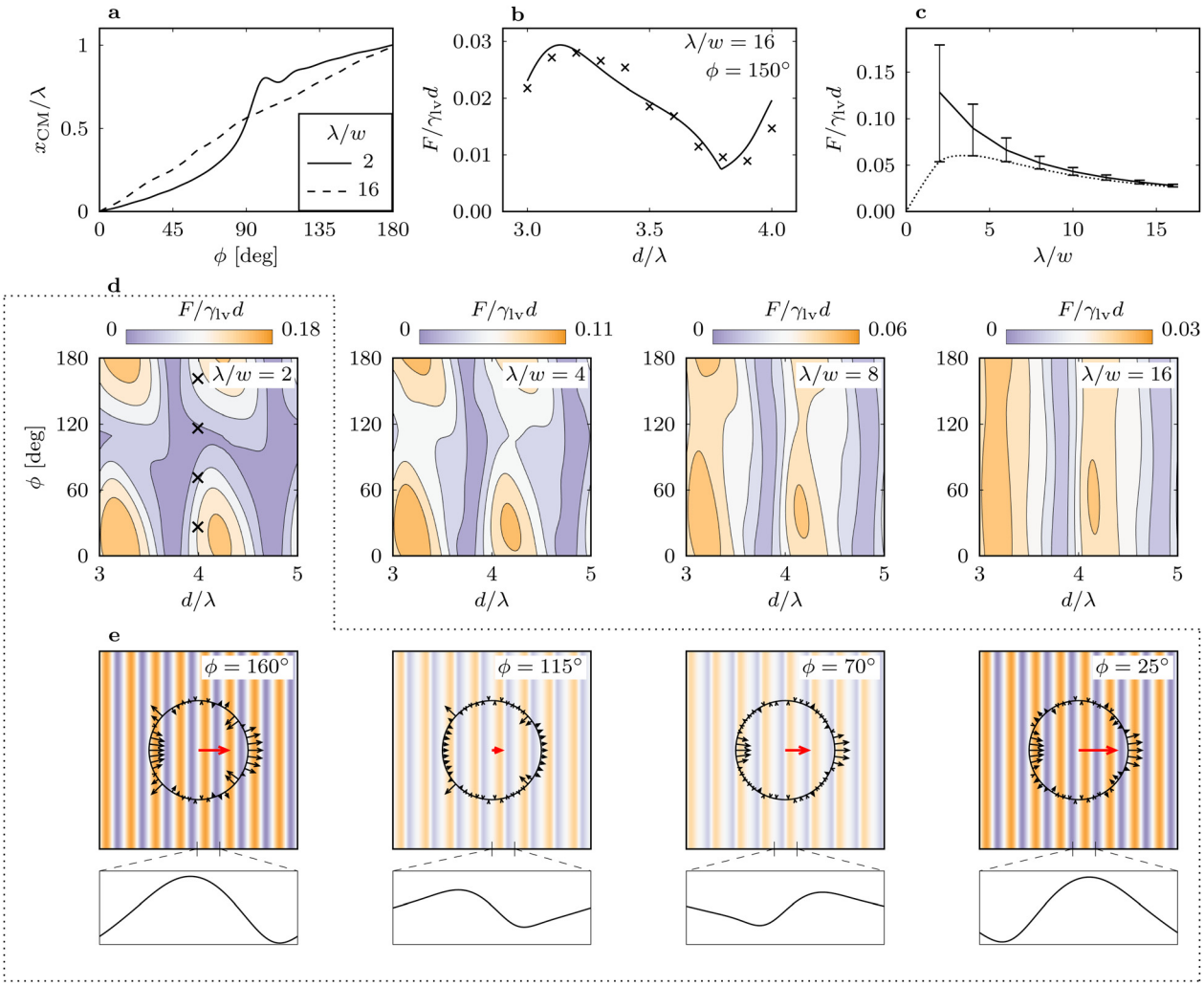

FIG. 5. Single-droplet transport on liquid crystal traveling surface waves. (a) Distance traveled by a single droplet (measured by the displacement of the center of mass x_{CM}), normalized with the wavelength as a function of the polarization angle. (b) The normalized dynamic-pinning force $F/d\gamma_{lv}$ as a function of the normalized diameter of the droplet, on a surface profile corresponding to $\phi = 150°$ and $\lambda/w = 16$. The crosses indicate numerical results, the solid line is the analytical result. (c) Mean (solid line), maximum and minimum of the dynamic-pinning force for ϕ between 0° and 180° as a function of λ/w, for $d/\lambda = 3.2$. The dotted line connects the minima. (d) Contour plots for the dynamic-pinning force as a function of both the normalized diameter of the droplet and the rotation angle ϕ for various values of λ/w. (e) Tensions along the three-phase line for different values of the polarization direction for $\lambda/w = 2$, corresponding to the crosses in (d) (left image). The color brightness represents the surface height, where vibrant colors represent a strongly corrugated surface.

perturbed contact angle at every point on the three-phase line is translated into a tension distribution and integrated to determine the total driving force (see Ref. 26 and Sec. II).

The efficiency gain from 0.1% to 100%, i.e., going from an average fluid velocity of 0.1% of the wave speed in the case of a single-fluid filled channel to slugs traveling along with the wave, was obtained with exactly the same light-driven surface wave. This did not include optimization of the channel height to obtain higher single-fluid velocities. The generated average velocity of the single fluid will increase when the amplitude of the wave increases, and ultimately it could reach the wave speed in extreme cases where the wave crests touch the other side of the channel. However, the slugs will always travel at the wave speed and consequently will always outperform the peristaltic method.

Because of the low switching frequency between the *cis* and *trans* states in currently available light-responsive liquid crystal polymers (~ 0.1 Hz), the wave speeds that can be generated in practice for typical wavelengths (10 s–100 s μm) are relatively low ($\sim 1 - 10\,\mu\text{m s}^{-1}$).[49] However, recent developments are promising, delivering larger deformations at faster response times.[28,42,50,51] In addition to the limitations in the actuation time, the response amplitude may also be of concern. In earlier studies, however, we have shown theoretically, numerically, and experimentally that amplitude-wavelength ratios down to $A/\lambda = 0.006$ were sufficient to generate enough force to drive individual droplets.[26]

On the other hand, for droplet propulsion, it is desirable to develop materials that have a high amplitude (relative to the wavelength), because the dimensionless driving force scales linearly with A/λ, see Sec. II [Eq. (A1)].

The dynamic-pinning forces generated by the mechanowetting effect have the intrinsic property that the driving force depends on the droplet or slug size, relative to the wavelength [see Figs. 4(e), 5(b), and 5(d)]. From Figs. 5(b) and 5(c), it becomes clear that the single surface used covers the range $F/\gamma_{lv}d \in [0.09, 0.28]$, i.e., a factor of 3 between the maximum and minimum. The underlying reason for the slug and droplet size-dependent efficiency is related to the specific position of the slug/droplet three-phase line relative to the surface topography. Near integer values of d/λ, the generated force along the three-phase line constructively adds up to the maximum force, whereas away from these integer values the amount of integrated force that is generated decreases considerably. This process varies continuously and can be expressed in a force landscape, as shown in Figs. 4(e) and 5(d) for the slugs and droplets, respectively. Note that the symmetrically shaped landscape in Fig. 4(e) is caused by the two-dimensional nature of the fluid slugs which have no variation in the out-of-plane direction, whereas the cause of the asymmetry in the landscape of Fig. 5(d) is due to the three-dimensional shape of the droplets. A consequence of the size-dependent transport efficiency is that the slug size or droplet size should be adjusted to the wavelength. However, when the size range of the to-be-transported droplets in the (microfluidic) system is known *a priori*, this can be taken into account in the design of the system. On the other hand, the size dependence can also be exploited for droplet sorting applications by utilizing the different transportation forces for differently sized droplets.[26]

When the results in this work are compared to the forces calculated in previous works, i.e., Refs. 26 and 27, we notice an increase in complexity. Our previous results were based on traveling waves with surface topographies that were only phase shifted in time (i.e., the vacuum pressed polydimethylsiloxane (PDMS) film in Ref. 26 and the sinusoidal wave in Ref. 27), while the current surfaces maintain their transporting capabilities despite the extensive morphological changes induced by the changing polarization angle. Because of this, the previous results show a much smoother transition between different values of d/λ and L/λ, while the current work, in particular Figs. 4(e) and 5(d), shows a more dynamic and complex dependence on d/λ, L/λ and λ/w. The reason for this is that different polarization states generate different wave structures, which may even (locally) generate different effective d/λ, so that a different maximum force is generated. As a consequence of this variation in efficiency with polarization angle, the net efficiency of the surface needs to be defined at the configuration that generates the lowest force (which according to our analysis is nonzero for all the configurations studied in the current work).

In applications of the presented transport mechanism, it can be desirable to optimize the director distribution in the liquid crystal film for mechanowetting forces that are larger and more consistent over the range of polarization angles. In the current study, the director distribution follows a continuously rotating pattern [which is sketched in Fig. 1(b)], such that the actuated part of the surface by the UV light is always the same, but phase shifted, resulting however in height profiles with varying mechanowetting forces. Using the theoretical and numerical models presented in this paper, the polarization angles and locations at which the mechanowetting forces are low can be identified and be used as input to the solid mechanics model presented in Ref. 40. Consequently, the director distribution can be adapted to increase the efficiency of the fluid transport, which can be achieved, e.g., by locally rotating the director or increasing the azobenzene density, depending on the outcome of the models.

V. CONCLUSION

In short, we have analytically and numerically demonstrated that traveling waves generated in azobenzene-enhanced liquid crystal films are able to transport fluids. We studied peristaltic fluid flow and fluid flow driven by fluid slugs through microfluidic channels and we analyzed the transport of individual droplets. Compared to peristaltic fluid flow, the fluid slugs are able to generate a continuous forward fluid flow (i.e., without back flow) at the speed of the wave so that the volumetric flow rates are two orders of magnitude larger. The traveling surface waves are able to transport the fluid slugs and droplets very efficiently by exploiting the dynamic three-phase line pinning to the wave front, achieving mean flow speeds that are equal to the wave speed. We anticipate that our results will provide new opportunities in utilizing traveling surface waves for fluid transport by means of light-controlled mechanowetting.

SUPPLEMENTARY MATERIAL

See the supplementary material for the other surface topographies and the nonphase-shifted data of Fig. 4(d).

AUTHORS' CONTRIBUTIONS

E.D.J. and R.K. performed fluid mechanics simulations. L.L. performed solid mechanics simulations. P.R.O. conceived and supervised the project. All authors discussed the results and E.D.J., R.K., and P.R.O. wrote the paper.

ACKNOWLEDGMENTS

This work was supported by NWO-TTW under Project No. 12826 and by the Dutch Polymer Institute under Project No. 775 "TOPSWITCH."

APPENDIX: LINEARIZATION OF THE FORCE-AMPLITUDE RELATION

Consider a simple one-dimensional waveform with amplitude A and wavelength λ, given by

$$h(x) = A\cos(x/\lambda).$$

Its partial derivative with respect to the x coordinate can be written as

$$\frac{\partial h}{\partial x} = -\frac{A}{\lambda}\sin(x/\lambda).$$

When substituted in Eq. (4), and considering that $F_x = F$, $A/\lambda \ll 1$, and $\arctan[u] \approx u$ for small values of u, we obtain its one-dimensional, linear form, i.e.,

$$\frac{F}{\gamma_{lv} d} = \frac{\sin\theta_Y}{2}\int_0^{2\pi} \cos(\varphi)\arctan\left[-\frac{A}{\lambda}\sin(x/\lambda)\right] d\varphi$$
$$\approx A\frac{\sin\theta_Y}{2\lambda}\int_0^{2\pi} -\cos(\varphi)\sin(d\cos(\varphi)/(2\lambda))\, d\varphi. \quad \text{(A1)}$$

DATA AVAILABILITY

The data that support the findings of this study are available from the corresponding author upon reasonable request.

REFERENCES

[1]D. Ishii, H. Horiguchi, Y. Hirai, H. Yabu, Y. Matsuo, K. Ijiro, K. Tsujii, T. Shimozawa, and T. Hariyama, "Water transport mechanism through open capillaries analyzed by direct surface modifications on biological surfaces," Sci. Rep. **3**, 3024 (2013).

[2]D. Li and Z. Guo, "Versatile superamphiphobic cotton fabrics fabricated by coating with SiO_2/FOTS," Appl. Surf. Sci. **426**, 271–278 (2017).

[3]S. Chatterjee, J. S. Murallidharan, A. Agrawal, and R. Bhardwaj, "Designing antiviral surfaces to suppress the spread of COVID-19," Phys. Fluids **33**, 052101 (2021).

[4]J. R. Castrejón-Pita, G. D. Martin, S. D. Hoath, and I. M. Hutchings, "A simple large-scale droplet generator for studies of inkjet printing," Rev. Sci. Instrum. **79**, 075108 (2008).

[5]G. M. Whitesides, "The origins and the future of microfluidics," Nature **442**, 368–373 (2006).

[6]A. Wixforth, "Acoustically driven planar microfluidics," Superlattices Microstruct. **33**, 389–396 (2003).

[7]L. Y. Yeo and J. R. Friend, "Ultrafast microfluidics using surface acoustic waves," Biomicrofluidics **3**, 012002 (2009).

[8]T. Dung Luong and N. Trung Nguyen, "Surface acoustic wave driven microfluidics—A review," Micro Nanosystems **2**, 217–225 (2010).

[9]P. Zhang, C. Chen, X. Su, J. Mai, Y. Gu, Z. Tian, H. Zhu, Z. Zhong, H. Fu, S. Yang, K. Chakrabarty, and T. J. Huang, "Acoustic streaming vortices enable contactless, digital control of droplets," Sci. Adv. **6**, eaba0606 (2020).

[10]Y. Wang, X. Tao, R. Tao, J. Zhou, Q. Zhang, D. Chen, H. Jin, S. Dong, J. Xie, and Y. Q. Fu, "Acoustofluidics along inclined surfaces based on AlN/Si Rayleigh surface acoustic waves," Sens. Actuators, A **306**, 111967 (2020).

[11]J. Berna, D. A. Leigh, M. Lubomska, S. M. Mendoze, E. M. Perez, P. Rudolf, G. Teobaldi, and F. Zerbetto, "Macroscopic transport by synthetic molecular machines," Nat. Mater. **4**, 704–710 (2005).

[12]M. K. Chaudhury and G. M. Whitesides, "How to make water run uphill," Science **256**, 1539–1541 (1992).

[13]N. Moradi, F. Varnik, and I. Steinbach, "Roughness-gradient-induced spontaneous motion of droplets on hydrophobic surfaces: A lattice Boltzmann study," Europhys. Lett. **89**, 26006 (2010).

[14]F. Varnik, M. Gross, N. Moradi, G. Zikos, P. Uhlmann, P. Müller-Buschbaum, D. Magerl, D. Raabe, I. Steinbach, and M. Stamm, "Stability and dynamics of droplets on patterned substrates: Insights from experiments and lattice Boltzmann simulations," J. Phys.: Condens. Matter **23**, 184112 (2011).

[15]J.-J. Huang, H. Huang, and X. Wang, "Numerical study of drop motion on a surface with stepwise wettability gradient and contact angle hysteresis," Phys. Fluids **26**, 062101 (2014).

[16]C. Liu, J. Li, C. Xiang, L. Che, Z. Wang, and X. Zhou, "Long-range spontaneous droplet self-propulsion on wettability gradient surfaces," Sci. Rep. **7**, 1–8 (2017).

[17]C. Lv, C. Chen, Y.-C. Chuang, F.-G. Tseng, Y. Yin, F. Grey, and Q. Zheng, "Substrate curvature gradient drives rapid droplet motion," Phys. Rev. Lett. **113**, 026101 (2014).

[18]M. S. Sadullah, G. Launay, J. Parle, R. Ledesma-Aguilar, Y. Gizaw, G. McHale, G. G. Wells, and H. Kusumaatmaja, "Bidirectional motion of droplets on gradient liquid infused surfaces," Commun. Phys. **3**, 166 (2020).

[19]H. Zhao, D. Orejon, K. Sefiane, and M. E. Shanahan, "Droplet motion and oscillation on contrasting micro-striated surfaces," J. Fluid Mech. **916**, A54 (2021).

[20]A. M. Pit, M. H. G. Duits, and F. Mugele, "Droplet manipulations in two phase flow microfluidics," Micromachines **6**, 1768–1793 (2015).

[21]G. Van der Veen and W. Prins, "Photomechanical energy conversion in a polymer membrane," Nature **230**, 70–72 (1971).

[22]M. G. Pollack, R. B. Fair, and A. D. Shenderov, "Electrowetting-based actuation of liquid droplets for microfluidic applications," Appl. Phys. Lett. **77**, 1725–1726 (2000).

[23]S. W. Walker, B. Shapiro, and R. H. Nochetto, "Electrowetting with contact line pinning: Computational modelling comparisons with experiments," Phys. Fluids **21**, 102103 (2009).

[24]K. Ichimura, S.-K. Oh, and M. Nakagawa, "Light-driven motion of liquids on a photoresponsive surface," Science **288**, 1624–1626 (2000).

[25]H. Dai, C. Gao, J. Sun, C. Li, N. Li, L. Wu, Z. Dong, and L. Jiang, "Controllable high-speed electrostatic manipulation of water droplets on a superhydrophobic surface," Adv. Mater. **31**, 1905449 (2019).

[26]E. de Jong, Y. Wang, J. M. J. den Toonder, and P. R. Onck, "Climbing droplets driven by mechanowetting on transverse waves," Sci. Adv. **5**, eaaw0914 (2019).

[27]E. de Jong, J. M. J. Den Toonder, and P. R. Onck, "Microfluidic slug transport on traveling-wave surface topographies by mechanowetting," Phys. Rev. Fluids **5**, 063604 (2020).

[28]D. Liu, L. Liu, P. R. Onck, and D. J. Broer, "Reverse switching of surface roughness in a self-organized polydomain liquid crystal coating," Proc. Natl. Acad. Sci. U. S. A. **112**, 3880–3885 (2015).

[29]D. Liu and D. J. Broer, "New insights into photoactivated volume generation boost surface morphing in liquid crystal coatings," Nat. Commun. **6**, 1–7 (2015).

[30]A. H. Gelebart, D. J. Mulder, M. Varga, A. Konya, G. Vantomme, E. W. Meijer, R. L. B. Selinger, and D. J. Broer, "Making waves in a photoactive polymer film," Nature **546**, 632–636 (2017).

[31]D. Han, Z. Lu, S. A. Chester, and H. Lee, "Micro 3D printing of a temperature-responsive hydrogel using projection micro-stereolithography," Sci. Rep. **8**, 1963 (2018).

[32]T. Wang, M. Farajollahi, Y. S. Choi, I.-T. Lin, J. E. Marshall, N. M. Thompson, S. Kar-Narayan, J. D. W. Madden, and S. K. Smoukov, "Electroactive polymers for sensing," Interface Focus **6**, 20160026 (2016).

[33]J. M. J. den Toonder and P. R. Onck, "Microfluidic manipulation with artificial/bioinspired cilia," Trends Biotechnol. **31**, 85–91 (2013).

[34]S. N. Khaderi, C. B. Craus, J. Hussong, N. Schorr, J. Belardi, J. Westerweel, O. Prucker, J. Ruhe, J. M. J. den Toonder, and P. R. Onck, "Magnetically-actuated artificial cilia for microfluidic propulsion," Lab Chip **11**, 2002–2010 (2011).

[35]J.-A. Lv, Y. Liu, J. Wei, E. Chen, L. Qin, and Y. Yu, "Photocontrol of fluid slugs in liquid crystal polymer microactuators," Nature **537**, 179–184 (2016).

[36]W. Li, X. Tang, and L. Wang, "Photopyroelectric microfluidics," Sci. Adv. **6**, eabc1693 (2020).

[37]C. Huang, J.-A. Lv, X. Tian, Y. Wang, Y. Ye, and J. Liu, "Miniaturized swimming soft robot with complex movement actuated and controlled by remote light signals," Sci. Rep. **5**, 17414 (2015).

[38]S. Palagi, A. G. Mark, S. Y. Reigh, K. Melde, T. Qiu, H. Zeng, C. Parmeggiani, D. Martella, A. Sanchez-Castillo, N. Kapernaum, F. Giesselmann, D. S. Wiersma, E. Lauga, and P. Fischer, "Structured light enables biomimetic swimming and versatile locomotion of photoresponsive soft microrobots," Nat. Mater. **15**, 647 (2016).

[39]D. Liu, C. Bastiaansen, J. den Toonder, and D. Broer, "Light-induced formation of dynamic and permanent surface topologies in chiral-nematic polymer networks," Macromolecules **45**, 8005–8012 (2012).

[40]L. Liu, D. J. Broer, and P. R. Onck, "Travelling waves on photo-switchable patterned liquid crystal polymer films directed by rotating polarized light," Soft Matter **15**, 8040–8050 (2019).

[41]L. Liu and P. R. Onck, "Topographical changes in photo-responsive liquid crystal films: A computational analysis," Soft Matter **14**, 2411–2428 (2018).

[42]L. Liu and P. R. Onck, "Enhanced deformation of azobenzene-modified liquid crystal polymers under dual wavelength exposure: A photophysical model," Phys. Rev. Lett. **119**, 057801 (2017).

[43]E. Berberović, N. P. van Hinsberg, S. Jakirlić, I. V. Roisman, and C. Tropea, "Drop impact onto a liquid layer of finite thickness: Dynamics of the cavity evolution," Phys. Rev. E **79**, 036306 (2009).

[44]A. Q. Raeini, M. J. Blunt, and B. Bijeljic, "Modelling two-phase flow in porous media at the pore scale using the volume-of-fluid method," J. Comput. Phys. **231**, 5653–5668 (2012).
[45]H. Rusche, "Computational fluid dynamics of dispersed two-phase flows at high phase fractions," Ph.D. thesis (Imperial College of Science, Technology and Medicine, 2002).
[46]H. Jasak, "Error analysis and estimation in the finite volume method with applications to fluid flows," Ph.D. thesis (Imperial College London, 1996).
[47]T. Young, "An essay on the cohesion of fluids," Philos. Trans. R. Soc. London **95**, 65–87 (1805).
[48]G. Taylor, "Analysis of the swimming of microscopic organisms," Proc. R. Soc. A **209**, 447–461 (1951).
[49]T. J. White and D. J. Broer, "Programmable and adaptive mechanics with liquid crystal polymer networks and elastomers," Nat. Mater. **14**, 1087–1098 (2015).
[50]D. Liu, C. W. M. Bastiaansen, J. M. J. den Toonder, and D. J. Broer, "Photo-switchable surface topologies in chiral nematic coatings," Angew. Chem. Int. Ed. **51**, 892–896 (2012).
[51]K. Mehta, A. R. Peeketi, J. A. Sol, M. G. Debije, P. R. Onck, and R. K. Annabattula, "Modeling of surface waves in photo-responsive viscoelastic liquid crystal thin films under a moving light source," Mech. Mater. **147**, 103388 (2020).